Measurement of the orbital angular momentum density of light by modal decomposition

Christian Schulze[1,4]**, Angela Dudley**[2]**, Daniel Flamm**[1]**, Michael Duparré**[1] **and Andrew Forbes**[2,3,4]

[1] Institute of Applied Optics, Abbe Center of Photonics, Friedrich Schiller University, Fröbelstieg 1, D-07743 Jena, Germany
[2] Council for Scientific and Industrial Research, National Laser Centre, PO Box 395, Pretoria 0001, South Africa
[3] School of Physics, University of KwaZulu-Natal, Private Bag X54001, Durban 4000, South Africa
E-mail: christian.schulze@uni-jena.de and aforbes1@csir.co.za

Abstract. We demonstrate a versatile method for the measurement of the orbital angular momentum (OAM) density of an optical field. By performing a modal decomposition with digital holograms, we reconstruct the full optical field from a small set of single-point intensity measurements, from which optical vortices, global OAM and OAM density can be derived. We validate the method on defined OAM-carrying beams yielding fidelities in the OAM density measurement of up to 99%, and subsequently apply the technique to unknown fields from optical fibers.

[S] Online supplementary data available from stacks.iop.org/NJP/15/073025/mmedia

[4] Authors to whom any correspondence should be addressed.

IOP Institute of Physics   Φ DEUTSCHE PHYSIKALISCHE GESELLSCHAFT

Contents

1. Introduction

It is well understood that light carries both a linear and an angular momentum [1, 2], and while the linear momentum per photon is related to the light beam's wavelength ($\hbar k$), the angular momentum per photon is an integer multiple of $\hbar$ [3]. The spin angular momentum component of light's total angular momentum has for long been associated with the polarization of light, and it was realized some 20 years ago that the orbital angular momentum (OAM) component was related to the spatial distribution of light [4]. Specifically, it was realized that the OAM of a light field could be customized by selecting a field with an azimuthal phase distribution of $\exp(\mathrm{i}l\phi)$, giving rise to an OAM of $l\hbar$ per photon. Such modes have been routinely generated in the laboratory and used for a plethora of applications [5, 6], notably in optical tweezers [7–9], communication studies [10, 11] and at the single-photon level for realizing high-dimensional entanglement [12–14]. As the latter necessitates the ability to measure multiple OAM states simultaneously, there has recently been progress toward the detection of OAM modes of light.

There are several options available for the detection of single OAM modes: the ubiquitous detection scheme involves operating the mode creation optics in reverse, e.g. the so-called fork holograms, and then projecting into a detectable Gaussian mode [12], a method that has seen an innovation recently by coupling vortex beams to plasmonic waves for detection [15]. Other solutions have involved diffraction off apertures [16–18], where the signal returned is indicative of the OAM spectrum, but this also requires analysis of a full two-dimensional (2D) interference pattern. Methods based on the rotational frequency shift [19–21] also exist but are rather complex to implement, while recent work on dove prism interferometers suggests a robustness for sorting odd and even OAM modes [22]. Recently, an efficient mode sorter [23, 24] has been proposed for the measurement of any OAM state as well as superposition states, and this has successfully been applied to Laguerre–Gaussian and Bessel OAM-carrying beams and their superpositions [25, 26]. Such sorters are ideal for detecting the presence of an OAM mode, even in a multimode field, but not for determining the intermodal phases of superposition fields. Without this information it is not possible to infer from the measurement the total OAM of the beam, nor the OAM density of the beam. Previous tools have considered

very specialized field distributions to measure the OAM density, e.g. Bessel beams, but would not be well suited to general fields with several modes involved [27].

In this paper, we demonstrate the measurement of the total OAM and OAM density of an arbitrary light field. We show that by modally decomposing the beam into an appropriate basis using a digital hologram, one can infer from only a few single-point intensity measurements the modal weightings and phases of any superposition, from which the OAM properties of the beam are directly accessible. Such a tool is ideally suited to classical light fields where many photons exist, and in particular to modal demultiplexing of OAM states in optical communication applications, either in free space or in fibers, and is considered to be of great significance in the fields of novel imaging [28] and particle manipulation [29] studies. To this end, we illustrate the technique on optical fibers after validating it on the measurement of structured light created with digital holograms.

2. Modal decomposition

Modal decomposition is a powerful tool for the detailed investigation of laser fields. Every optical field can be conceived as quantized by a number of modes. Such modes may have a physical presence as in the case of laser resonators [30] or optical fibers [31], which allow the oscillation or propagation of only discrete field distributions, the so-called modes. Alternatively, modes may merely be used as a different (mathematical) description of a laser field, allowing a detailed beam analysis, but without physical relevance of the mode content [32, 33].

Mathematically, any optical field can be expressed in terms of modes, which constitute orthogonal basis functions:

$$\mathbf{U}(\mathbf{r}) = \sum_{l=1}^{N} c_l \Psi_l(\mathbf{r}) \tag{1}$$

with $\mathbf{r} = (x, y)$ the spatial coordinates, $c_l = \rho_l \, e^{i\Delta\phi_l}$ the complex expansion coefficient with amplitude ρ_l and intermodal phase $\Delta\phi_l$ (with respect to a reference phase), $\Psi_l(\mathbf{r})$ the lth mode field, which can be vector valued, and N the number of modes. Beam intensity $I(\mathbf{r})$ and phase $\Phi(\mathbf{r})$ are easily inferred from the modal amplitudes and phases via

$$I(\mathbf{r}) = |\mathbf{U}(\mathbf{r})|^2, \tag{2}$$

$$\Phi_j(\mathbf{r}) = \arg\left[U_j(\mathbf{r})\right], \tag{3}$$

where Φ_j is the respective phase of the field component U_j. The modal decomposition of a laser field as described by equation (1) can be performed all-optically using correlation filters [34, 35]. Such a filter performs a correlation of the incident field with modes that are encoded into the filter, which allows us to measure the power and relative phase of each individual mode from an inner product measurement [36, 37]. This ability is based on the specific design of the transmission function of the holographic device that constitutes the correlation filter. This transmission function varies with the quantity that needs to be measured. Measuring the power of a distinct mode requires the complex conjugate of that very mode to be encoded as transmission function [35]

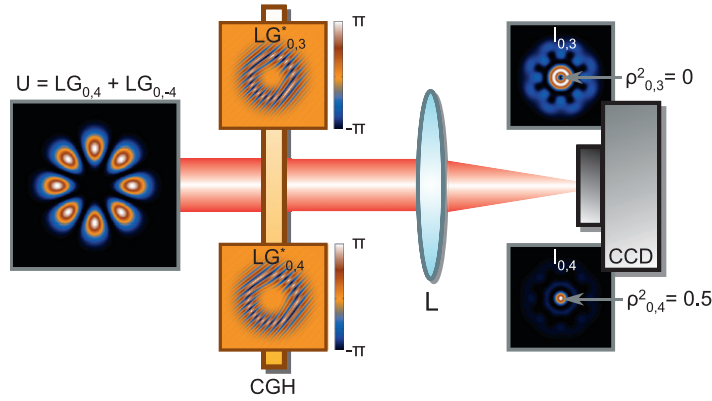$$T_l(\mathbf{r}) = \Psi_l^*(\mathbf{r}), \tag{4}$$

Figure 1. Scheme of the inner product measurement employing the correlation filter, a $2f$ configuration and a camera. Exemplarily, the analysis of an in-phase superposition of equally weighted Laguerre–Gaussian modes $LG_{0,4} + LG_{0,-4}$ is shown. Displaying transmission functions equal to $LG^*_{0,3}$ and $LG^*_{0,4}$ yields correlation signals $I_{0,3}$ and $I_{0,4}$ as well as relative modal powers $\rho^2_{0,3}$ and $\rho^2_{0,4}$. With the transmission functions superposed gratings enable signal separation from undiffracted light.

where '*' denotes the complex conjugation. Using this transmission function for performing the inner product measurement yields an intensity on the optical axis in the Fourier plane of the correlation filter that is $\propto \rho^2_l$. Hence, from a simple intensity measurement the power of a mode can be inferred.

Similarly, the unambiguous measurement of the phase difference of a mode to a chosen reference mode $\Delta\phi_l$ necessitates encoding a superposition of the mode field with the reference field into the match filter [35]:

$$
\begin{aligned}
T_l^{\cos}(\mathbf{r}) &= [\Psi_0^*(\mathbf{r}) + \Psi_l^*(\mathbf{r})]/\sqrt{2}, \\
T_l^{\sin}(\mathbf{r}) &= [\Psi_0^*(\mathbf{r}) + i\Psi_l^*(\mathbf{r})]/\sqrt{2}.
\end{aligned}
\tag{5}
$$

Accordingly, the intermodal phase $\Delta\phi_l$ can be calculated by [35]

$$
\Delta\phi_l = -\arctan\left[\frac{2I_l^{\sin} - \rho_l^2 - \rho_0^2}{2I_l^{\cos} - \rho_l^2 - \rho_0^2}\right],
\tag{6}
$$

where $I_l^{\sin}$ and $I_l^{\cos}$ depict the intensity signals from the inner product (phase) measurements. Physically, such filters can be implemented using a phase-only spatial light modulator (SLM) [34] or solid amplitude-only filters [35] by employing special coding techniques to transfer the complex-valued transmission function to a phase-only [38] or an amplitude-only function [39], respectively.

The procedure of the inner product measurement is shown schematically in figure 1. Consider e.g. a superposition of two equally weighted Laguerre–Gaussian modes $(LG_{0,4} + LG_{0,-4})/\sqrt{2}$ with azimuthal orders of $+4$ and -4, but zero radial order, illuminating the correlation filter. Displaying a transmission function $T = LG^*_{0,3}$ (e.g. encoded on an SLM) yields an intensity minimum at the center of the optical axis in the Fourier plane of the match filter as realized by a $2f$ setup and measured with a camera. Hence, the correlation signal $I_{0,3} \propto \rho^2_{0,3}$ is zero. However, if the field of a mode is displayed as a transmission function that is actually

IOP Institute of Physics Φ DEUTSCHE PHYSIKALISCHE GESELLSCHAFT

contained in the beam, e.g. $T = \mathrm{LG}_{0,4}^*$, a non-zero correlation signal appears, yielding a relative modal power of $\rho_{0,4}^2 = 0.5$ (cf figure 1).

The correlation filter can only correlate scalar, i.e. homogeneously polarized, fields. In the general case of vector beams with spatially varying polarization, a complete description of the optical field **U** is provided by the subsequent analysis of the Cartesian field components U_x and U_y, including the proper phase difference δ between them.

This can be done by determination of the Stokes parameters $S_0 \ldots S_3$ of the beam, which necessitates six (assuming completely polarized light) modal decomposition measurements with a quarter-wave plate and a polarizer in appropriate orientations in front of the hologram [40–42]:

$$
\begin{aligned}
S_0 &= |U_x|^2 + |U_y|^2 = I(0°) + I(90°), \\
S_1 &= |U_x|^2 - |U_y|^2 = I(0°) - I(90°), \\
S_2 &= 2|U_x||U_y|\cos\delta = I(45°) - I(135°), \\
S_3 &= 2|U_x||U_y|\sin\delta = I_{\lambda/4}(45°) - I_{\lambda/4}(135°).
\end{aligned}
\tag{7}
$$

Each field transmitted by a quarter-wave plate and a polarizer is modally decomposed and the beam intensity is reconstructed following equation (2). Accordingly, $I(\alpha)$ are the reconstructed intensities behind the polarizer at angular orientations $\alpha = 0°, 45°, 90°, 135°$, and $I_{\lambda/4}(\alpha)$ denote two additional measurements with the polarizer placed at $\alpha = 45°, 135°$ behind a preceding quarter-wave plate. Performing the depicted six modal decompositions, information on the optical field is complete, including amplitude, phase and polarization distribution.

3. Orbital angular momentum density

As shown in the previous section, modal decomposition using a correlation filter yields complete information about the optical field. Hence, the Poynting vector distribution **P**(**r**) can be calculated by [32]

$$
\mathbf{P}(\mathbf{r}) = \frac{1}{2}\Re\left[\frac{\mathrm{i}}{\omega\epsilon_0}\epsilon^{-1}(\mathbf{r})[\nabla \times \mathbf{U}(\mathbf{r})] \times \mathbf{U}^*(\mathbf{r})\right]
\tag{8}
$$

for vector fields **U**, and by [43]

$$
\mathbf{P}(\mathbf{r}) = \frac{\epsilon_0\omega}{4}\left[\mathrm{i}(U\nabla U^* - U^*\nabla U) + 2k|U|^2\mathbf{e}_z\right]
\tag{9}
$$

for scalar fields U, where ω is the angular frequency, ϵ is the permittivity, ϵ_0 is the permittivity of vacuum, $k = 2\pi/\lambda$ is the wave number and $\mathbf{e}_z$ is the z-direction. From the Poynting vector, the OAM density is accessible from [44]

$$
\mathbf{j} = \mathbf{r} \times \frac{\mathbf{P}}{c^2}.
\tag{10}
$$

Hence, the OAM density is measurable for both scalar and vector fields, using the modal decomposition principle as outlined in section 2. In the following, only the z-component j_z, which is of most relevance for application, is considered and termed 'OAM density'.
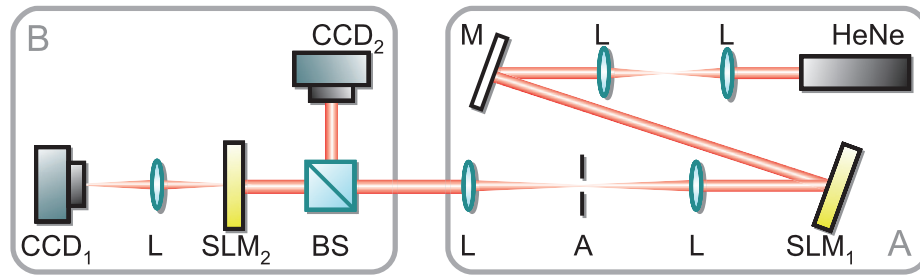
Figure 2. Experimental setup for the generation and characterization of Laguerre–Gaussian beams of different order. HeNe: helium–neon laser; L: lens; M: mirror: SLM$_{1,2}$: spatial light modulators; A: aperture; CCD$_{1,2}$: CCD cameras; BS: beam splitter.

4. Investigation of Laguerre–Gaussian beams

Laguerre–Gaussian modes are well known to carry OAM, which has made them the predominant object of investigation in recent years [5, 6]. Hence, they depict a well-suited example to prove the procedure for determining the OAM density as described in sections 2 and 3.

4.1. Experimental setup

The experimental setup for measuring these defined OAM states consisted of a branch for beam generation (A) and their subsequent analysis (B), as depicted in figure 2. To generate the various Laguerre–Gaussian beams, for which we intended to calculate the OAM density, a helium–neon laser (linearly polarized) was expanded through a telescope and directed onto the first SLM (reflective, HoloEye, PLUTO-VIS, 1920×1080 pixels of pitch $8\,\mu$m). By displaying the respective mode fields on SLM$_1$ using the coding technique as described in [34, 38], the corresponding beams were generated in the first diffraction order with the same linear polarization as the seed laser. The beam plane of SLM$_1$ was relay imaged through a beam splitter (BS) to a near-field CCD camera directly recording the beam intensity, CCD$_2$ (Spiricon, USB-SP620U), and a second SLM (SLM$_2$, same specifications as SLM$_1$), which was used to perform the inner product measurement to find the modal powers ρ_l^2 and intermodal phases $\Delta\phi_l$ as described in section 2. An aperture in the Fourier plane of SLM$_1$ was used to select the first diffraction order and block all the remaining ones. The diffracted field from SLM$_2$ was Fourier transformed by a single lens in $2f$ configuration and the correlation signal was detected by CCD$_1$ (PGR Scorpion, SCOR-20SOM). The modal decomposition was performed by displaying the transmission functions of equations (4) and (5) on SLM$_2$ subsequently, and recording the correlation signal in the Fourier plane at CCD$_1$, which yields the modal powers ρ_l^2 and phases $\Delta\phi_l$, and hence the optical field (equation (1)), the Poynting vector (equations (8) and (9)) and the OAM density (equation (10)). Note that displaying the single transmission functions in sequence, using the flexibility of the SLM, allows a large number of modes to be tested, hence allowing the characterization of optical fields with high spatial frequencies. The number of modes is limited for practical reasons by the measurement time and beam stability, and the weakness of the correlation signal, which needs to be distinguished from noise, in the
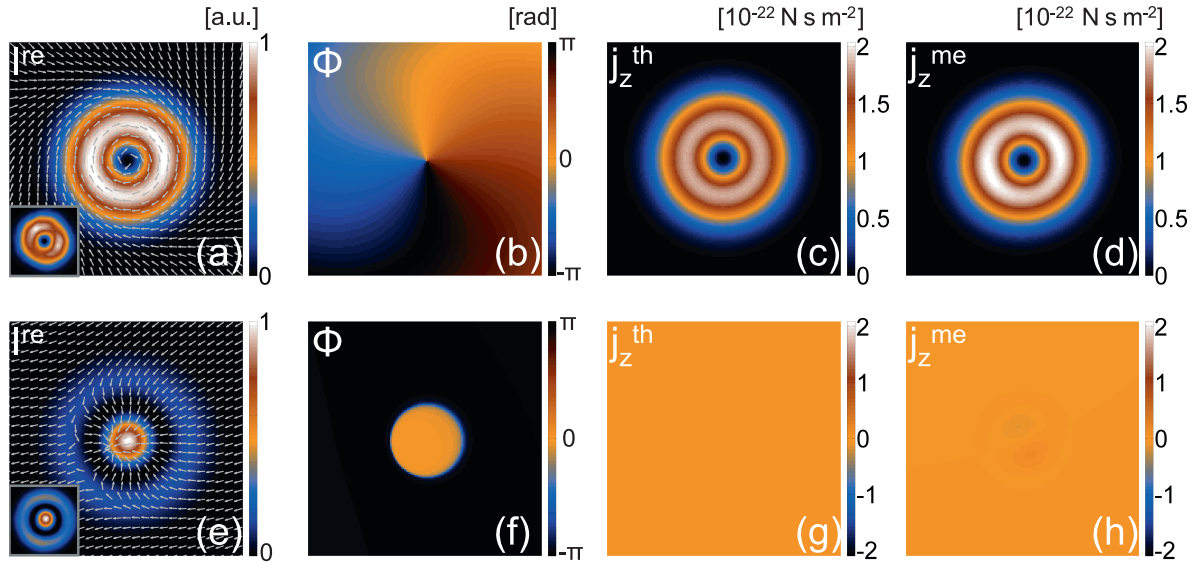
Figure 3. Characterization of pure Laguerre–Gaussian modes. (a)–(d) Reconstructed intensity with transverse Poynting vectors, reconstructed phase, theoretical OAM density and measured OAM density, respectively, of an $LG_{0,1}$ mode beam. (e)–(h) Same for the $LG_{1,0}$ beam. OAM densities in $N\,s\,m^{-2}$. Insets in (a) and (e) depict measured beam intensities, respectively.

case of too many modes. For the following experiments, we decomposed the beam into as many as 30 modes (three hologram patterns for each mode; see equations (4) and (5)) with a total measurement time of about 10 s. The temporal effort can be reduced significantly by combining them in sequence measurements with the well-known angular multiplexing approach.

4.2. Results

To verify the procedure as described in sections 2 and 3, Laguerre–Gaussian beams of known OAM density (calculable using equations (8) and (10)) were generated, which served as a reference to the modal decomposition results. Thereby, we decomposed the beam into a broad mode spectrum each time, pretending to not know which beam we were investigating. Since all Laguerre–Gaussian sample beams were generated with linear polarization, one decomposition experiment was enough to determine the OAM density of each beam and the Stokes measurement according to equation (7) was not necessary.

As a first example, a pure Laguerre–Gaussian mode $LG_{0,1}$ was generated with SLM_1, where the last-mentioned index indicates the order of the helical phase and the topological charge [6, 45]. To measure the mode content of this beam, Laguerre–Gaussian mode patterns with p ranging from 0 to 2 and l ranging from -4 to 4 were displayed subsequently on SLM_2 and the correlation signals were measured. Accordingly, the purity of the $LG_{0,1}$ mode amounts to 99.6% of relative mode power. Additionally, the intermodal phases were determined by displaying previously stated mode patterns in superposition with the LG_{00} mode (equation (5)), which served as the reference mode. Using equation (1), the optical field was reconstructed from the measured modal amplitudes and phases. Figure 3 depicts the results of the beam characterization: figure 3(a) shows the reconstructed intensity (equation (2)), which reveals

the typical donut shape with an intensity minimum in its center indicating phase singularity. As an inset, the directly measured intensity (near field) reveals very good agreement with the reconstruction. Regarding the phase reconstruction of the beam (equation (3)) in figure 3(b), the helical phase structure is clearly visible, proving the presence of phase singularity in the beam center.

Applying the procedure of section 3 to the beam under investigation, the Poynting vector and OAM density are derived. In figure 3(a), the transverse components of the Poynting vector are depicted as an arrow plot on top of the reconstructed intensity, revealing the spiralling nature for a beam with an azimuthal phase structure [47, 48]. Figures 3(c) and (d) illustrate theoretical and measured OAM densities for the beam under test. Both densities agree very well (a 2D correlation coefficient of 99%) and resemble the intensity of the beam, which can be viewed as a characteristic of Laguerre–Gaussian beams and is a logical consequence of equations (9) and (10). Hence, similar to the intensity distribution, the OAM density is zero at the position of the phase singularity and increases to a ring-shaped maximum. Remarkably, the OAM density is exclusively positive. However, this fact can be easily understood, considering that the z-component of the OAM density is proportional to the φ-component of the Poynting vector, and hence to the azimuthal index l (here $l = +1$), provided the beam carries a helical phase [43]. Moreover, it becomes clear that our presented technique is capable of measuring the OAM density quantitatively. Here, the maximum is found to be $2.04 \times 10^{-22}\,\mathrm{N\,s\,m^{-2}}$.

The results of figure 3 show that a beam having a helical phase structure has a non-zero OAM density distribution, which mainly follows the intensity distribution. However, Laguerre–Gaussian beams with an azimuthal index $l = 0$ will have a vanishing φ-component of the Poynting vector P_φ [43], and consequently a vanishing OAM density. To prove this relation, a Laguerre–Gaussian mode $\mathrm{LG}_{1,0}$ was generated and characterized analogously to the previous experiment. The corresponding results are depicted in figures 3(e)–(h). Again, reconstructed and measured beam intensities correlate very well (figure 3(e)). The reconstructed phase distribution in figure 3(f) reveals the typical circular phase jump of π between the inner and outer beam parts. Figures 3(g) and (h) picture the measured and calculated OAM densities, which are both zero, which is reasonable, since the beam does not contain any azimuthal phase component.

Thus far the investigated beams have been single Laguerre–Gaussian modes. However, even more interesting with regard to the conservation of momentum and topological charge are mode superpositions [45, 46]. By way of example, we examined a superposition of two Laguerre–Gaussian beams $\mathrm{LG}_{0,1} + \mathrm{LG}_{0,-2}\,\mathrm{e}^{-\mathrm{i}\pi/3}$ with an intermodal phase shift of $\Delta\phi = -\pi/3$. The results are depicted in figure 4. Reconstructed and measured intensities both reveal the three-lobe structure formed by the interference of the two modes (figure 4(a)). The reconstructed phase distribution (figure 4(b)) unveils four singularities: one in the beam center of topological charge $l = +1$, and three symmetrically surrounding the center with an azimuthal separation of $120°$, each having a charge of $l = -1$. The positions of the singularities are visible from the arrow plot of the transverse Poynting vector in figure 4(a) as well, which illustrates that the Poynting vector spirals around four rotation centers depicting the singularities (marked with red dots). It is interesting to note that in contrast to the total angular momentum, the number of singularities and the total topological charge are not conserved when combining two OAM-carrying beams [45, 46]. The interference creates new features: whereas the separate beams contain one singularity each, with charges $+1$ and -2, respectively, the combined beam exhibits four singularities and the total topological charge is -2. Hence both the number of singularities and the total charge are not additive.
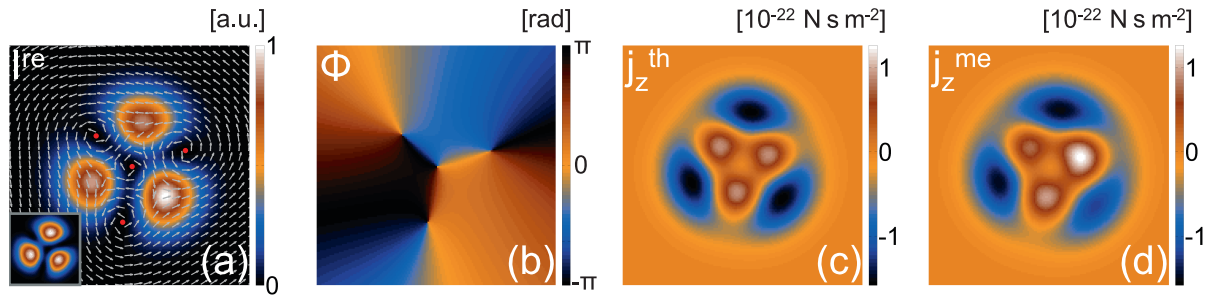
Figure 4. Characterization of a Laguerre–Gaussian beam $LG_{0,1} + LG_{0,-2}\,e^{-i\pi/3}$. (a) Reconstructed intensity and transverse Poynting vectors (red dots mark the position of the phase singularities). (b) Reconstructed phase. (c) Theoretical OAM density. (d) Measured OAM density. OAM densities in N s m^{-2}. The inset in (a) depicts the measured beam intensity.
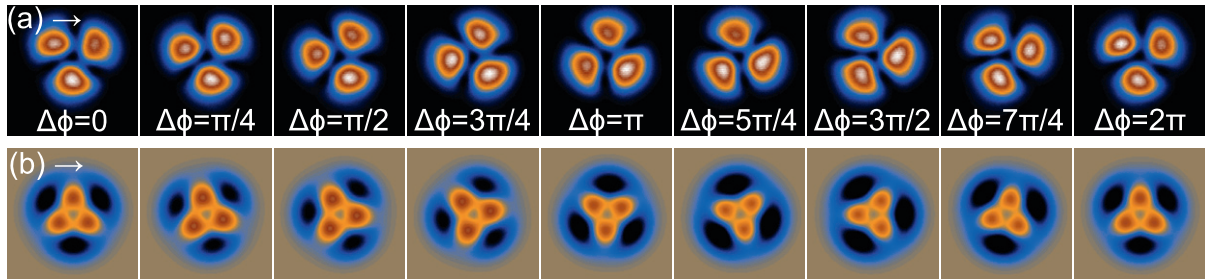

Figure 5. Rotation of the beam intensity (a) and of the OAM density (b) of the superposition $LG_{0,1} + LG_{0,-2}\,e^{i\Delta\phi}$ while changing the intermodal phase difference $\Delta\phi = 0 \ldots 2\pi$ yielding a rotation of 120°. Rotation in full resolution, see movie 1 in the supplementary data (available from stacks.iop.org/NJP/15/073025/mmedia).

Figures 4(c) and (d) depict the measured and calculated OAM densities, which correlate well by 92% (2D correlation coefficient). Since the azimuthal indices of the involved modes are of positive and negative sign ($l = 1$ and -2), the resulting OAM density exhibits positive and negative values as well. Moreover, the structure of the OAM density resembles the triangular symmetry of the intensity distribution with maxima in the vicinity of the phase singularities.

A generalization of the previously studied beam is achieved by introducing an arbitrary phase shift between the two modes $LG_{0,1} + LG_{0,-2}\,e^{i\Delta\phi}$. As the intermodal phase difference is varied from 0 to 2π by changing the phase pattern on SLM_1, the beam rotates by 120° as visible in figure 5, where $\Delta\phi$ was changed in steps of $\pi/4$. The full resolution video (steps of $\pi/20$) can be viewed in figure 5 (movie 1). At each step in the intermodal phase, a complete modal decomposition was performed to measure the OAM density. Accordingly, it can be seen that the beam intensity rotates in common with the OAM density. Regarding the phase structure, the three singularities of charge -1 rotate around the singularity in the center with topological charge $+1$. Figure 6 depicts the measured position of all four singularities as a function of intermodal phase difference $\Delta\phi$ yielding a threefold helix around a static central line, as determined by a tracking routine from the measured phase distributions. Projecting the singularity movement onto the x–y plane (inset in figure 6), it becomes clear that the three outer
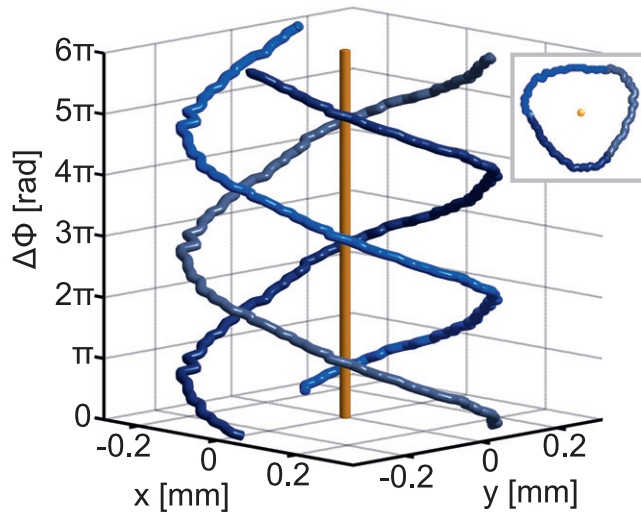
Figure 6. Measured movement of the four phase singularities as a function of the intermodal phase shift $\Delta\phi$ in the superposition $\mathrm{LG}_{0,1} + \mathrm{LG}_{0,-2}\, e^{i\Delta\phi}$. The inset depicts the top view.
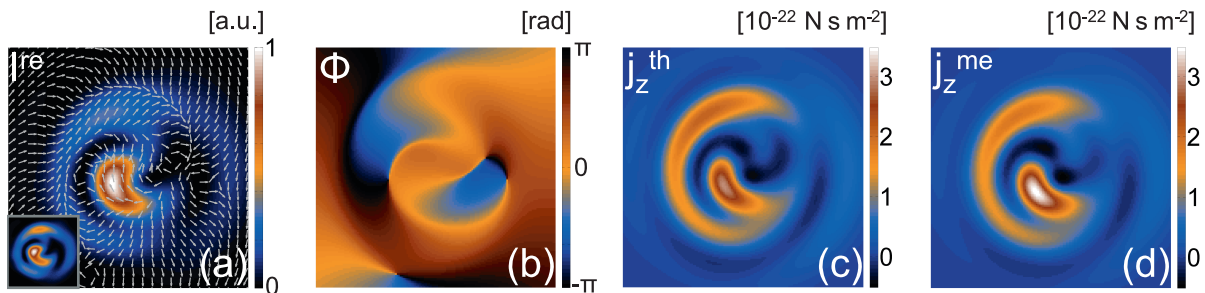

Figure 7. Characterization of a superposition of five Laguerre–Gaussian modes $\mathrm{LG}_{0,0} + \mathrm{LG}_{1,1}\, e^{i\pi/4} + \mathrm{LG}_{2,2}\, e^{i\pi/3} + \mathrm{LG}_{2,0}\, e^{i\pi/2} + \mathrm{LG}_{0,2}\, e^{i\pi}$. (a) Reconstructed intensity. (b) Reconstructed phase. (c) Theoretical OAM density. (d) Measured OAM density. OAM densities are in $\mathrm{N\,s\,m}^{-2}$. The inset in (a) depicts measured beam intensity.

singularities do not move on a circle, but more on a curve resembling a contour line stretched around the three intensity lobes of the beam.

A more complicated example, depicting an arbitrary mode superposition, is shown in figure 7, where five Laguerre–Gaussian modes have been superposed, $\mathrm{LG}_{0,0} + \mathrm{LG}_{1,1}\, e^{i\pi/4} + \mathrm{LG}_{2,2}\, e^{i\pi/3} + \mathrm{LG}_{2,0}\, e^{i\pi/2} + \mathrm{LG}_{0,2}\, e^{i\pi}$, each with a distinct intermodal phase, yielding an asymmetric beam profile, and a phase distribution that contains four singularities. Again, it can be seen that the total topological charge is not additive, as is the number of singularities.

The uncertainty of the OAM measurements can be inferred from the uncertainty in the measurement of modal amplitudes and phases, which are known from statistical evaluations to amount to 1% of total power and to 5° in terms of the modal phase. Accordingly, the OAM error depends on the number of modes and on the mode fields involved in the superposition, yielding a value for the above cases of about $0.2 \times 10^{-22}\,\mathrm{N\,s\,m}^{-2}$, averaged over the beam diameter.
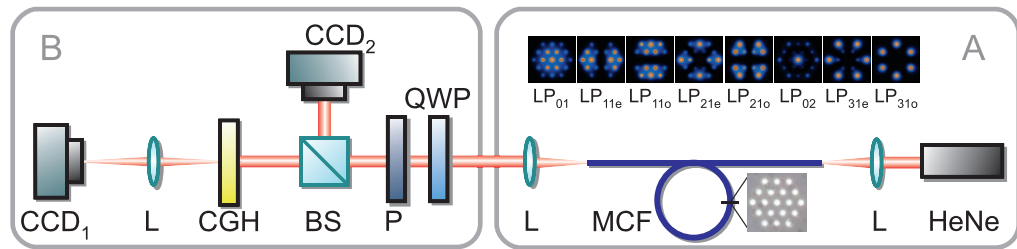
Figure 8. Experimental setup for measuring the OAM density of a fiber beam. HeNe: helium–neon laser; L: lens; MCF: multicore fiber; QWP: quarter-wave plate; P: polarizer; BS: beam splitter; CGH: computer-generated hologram; $CCD_{1,2}$: CCD cameras. Insets depict the modes and a cross section of the fiber.

5. Investigation of fiber beams

The comparison of the measured OAM densities with those expected for the artificially generated reference beams proved that the presented technique yields accurate results regarding shape and absolute scale. Hence, the method can be applied to unknown laser beams, for which no reference can be provided. Suitable examples are beams emerging from optical multimode fibers, which have been studied to generate controllable OAM states [49, 50]. Instead of programming modes and mode superpositions on a separate SLM for beam generation, the optical field is here created naturally by multimode interference inside the fiber, generally yielding complex phase and polarization properties.

5.1. Experimental setup

Correspondingly, the experimental setup was changed according to figure 8. As a beam source, a multimode fiber with 19 hexagonally arranged cores embedded in a common cladding material (single core diameter $2.2\,\mu$m, core-to-core distance $5.5\,\mu$m, single core numerical aperture NA $= 0.108$) and guiding ten transverse modes was seeded with the fundamental Gaussian beam of a helium–neon laser ($\lambda = 633$ nm). The modes of the fiber and a microscope image of its end facet under white light illumination are illustrated in figure 8 as insets. The fiber output was relay imaged (4f imaged) to the correlation filter, which in this experiment was a static binary amplitude-only computer-generated hologram (CGH), as used by Kaiser *et al* [35], and necessitating a different coding technique [39]. Since the fiber under test generally creates fields with spatially varying polarization, we measured all the Stokes parameters of the beam as described by equation (7), employing a quarter-wave plate and a polarizer, yielding complete information on the vector field including amplitude, phases and polarization. As in the previous experiments with Laguerre–Gaussian beams, a 2f setup behind the CGH (previously SLM) enabled the correlation measurement with a CCD camera (CCD_1). Again, a beam splitter in front of the hologram and a second CCD camera (CCD_2) provided direct recording of the beam intensity.

5.2. Results

Figure 9 illustrates an example of a fiber beam consisting of 10% $LP_{0,1}$, 4% $LP_{1,1,e}$, 2% $LP_{1,1,o}$, 39% $LP_{2,1,e}$, 31% $LP_{2,1,o}$, 5% $LP_{0,2}$, 4% $LP_{3,1,e}$ and 2% $LP_{3,1,o}$. As outlined by
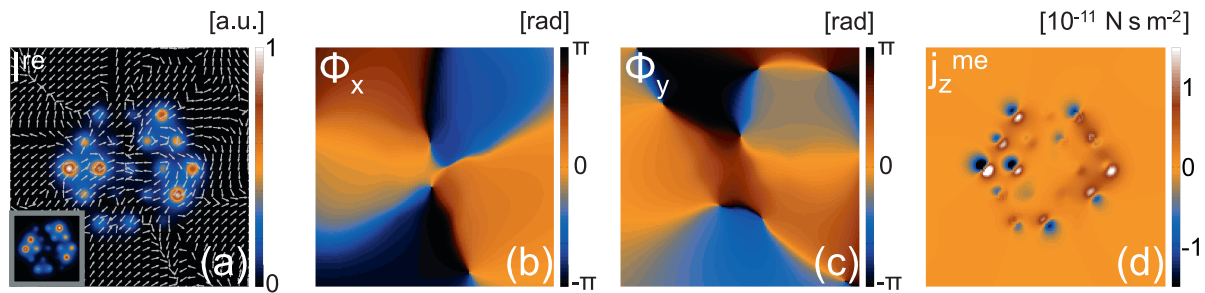
Figure 9. Characterization of a fiber beam consisting of a superposition of ten modes of a multicore fiber (10% LP_{01}, 4% LP_{11e}, 2% LP_{11o}, 39% LP_{21e}, 31% LP_{21o}, 5% LP_{02}, 4% LP_{31}, 2% LP_{31}). (a) Measured near-field intensity. (b) Reconstructed phase structure of the x-component of the field. (c) Reconstructed phase structure of the y-component of the field. (d) Measured OAM density. The inset in (a) depicts measured beam intensity.

figure 9(a), the reconstructed beam intensity reveals good agreement with the direct intensity measurement. Note that both intensities represent the sum of intensities recorded in the x- and y-polarization directions as selected with the polarizer (cf figure 8). Figures 9(b) and (c) depict the reconstructed phase distributions in the x- and y-directions, containing multiple phase singularities and phase steps. The reconstructed OAM density, illustrated in figure 9(d), reveals many hot spots that are located at the positions of the single cores. This is reasonable, since the OAM density is proportional to the gradients of the field in the x- and y-directions [45], which are largest at the interfaces of the cores with the common fiber cladding. Hence, dipole-like OAM structures appear at the core positions. Apparently, the OAM density is much larger than in the previous cases, of the order of $1 \times 10^{-11}\,\mathrm{N\,s\,m^{-2}}$. This is a logical consequence of the much smaller dimension of the beam, which is roughly extended to within a diameter of 25 μm.

6. Summary and conclusion

In summary, we have demonstrated a novel measurement system to quantify the OAM density of light. The technique is based on correlation filters to perform a modal decomposition with subsequent reconstruction of the optical field, which allows one to derive the Poynting vector and the OAM density using a simple relationship. The method stands out due to its easy setup, necessitating only an appropriate hologram, a lens and a single point detector. Laguerre–Gaussian beams of different orders were generated with an SLM and served as reference beams of known OAM density to validate the technique. Both measured and theoretically expected OAM densities are in very good agreement, hence proving the accuracy of the technique, yielding measurement fidelities of up to 99%. As an application case, the method was used to characterize a vector beam emerging from a multimode optical fiber. In consequence, the correlation filter method is easily applicable to scalar and vector fields and allows the characterization of the OAM density in an easy and fast manner. Accordingly, the presented technique depicts a versatile tool in many OAM-based applications, such as optical communication and particle manipulation.

Acknowledgment

References

[1] Poynting J H 1909 The wave motion of a revolving shaft and a suggestion as to the angular momentum in a beam of circularly polarised light *Proc. R. Soc. Lond.* A **82** 560–7

[2] Beth R A 1936 Mechanical detection and measurement of the angular momentum of light *Phys. Rev.* **50** 115–25

[3] Demore C, Yang Z, Volovick A, Cochran S, MacDonald M and Spalding G 2012 Mechanical evidence of the orbital angular momentum to energy ratio of vortex beams *Phys. Rev. Lett.* **108** 194301

[4] Allen L, Beijersbergen M W, Spreeuw R J C and Woerdman J P 1992 Orbital angular-momentum of light and the transformation of Laguerre–Gaussian laser modes *Phys. Rev.* A **45** 8185–9

[5] Allen L, Padgett M J and Babiker M 1999 The orbital angular momentum of light *Progress in Optics* vol 39 (Amsterdam: North-Holland) chapter 4, pp 291–372

[6] Yao A M and Padgett M J 2011 Orbital angular monentum: origins, behavior and applications *Adv. Opt. Photon.* **3** 161–204

[7] He H, Friese M E J, Heckenberg N R and Rubinsztein-Dunlop H 1995 Direct observation of transfer of angular momentum to absorptive particles from a laser beam with a phase singularity *Phys. Rev. Lett.* **75** 826–9

[8] Simpson N B, Dholakia K, Allen L and Padgett M J 1997 Mechanical equivalence of spin and orbital angular momentum of light: an optical spanner *Opt. Lett.* **22** 52–4

[9] Padgett M J and Bowman R 2011 Tweezers with a twist *Nature Photon.* **5** 343–8

[10] Gibson G, Courtial J, Padgett M J, Vasnetsov M, Pasko V, Barnett S M and Franke-Arnold S 2004 Free-space information transfer using light beams carrying orbital angular momentum *Opt. Express* **12** 5448–56

[11] Wang J *et al* 2012 Terabit free-space data transmission employing orbital angular momentum multiplexing *Nature Photon.* **6** 488–96

[12] Mair A, Vaziri A, Weihs G and Zeilinger A 2001 Entanglement of the orbital angular momentum states of photons *Nature* **412** 313–6

[13] Dada A C, Leach J, Buller G S, Padgett M J and Andersson E 2011 Experimental high-dimensional two-photon entanglement and violations of generalized Bell inequalities *Nature Phys.* **7** 677–80

[14] Leach J, Jack B, Romero J, Jha A K, Yao A M, Franke-Arnold S, Ireland D G, Boyd R W, Barnett S M and Padgett M J 2010 Quantum correlations in optical angle-orbital angular momentum variables *Science* **329** 662–5

[15] Genevet P, Lin J, Kats M A and Capasso F 2012 Holographic detection of the orbital angular momentum of light with plasmonic photodiodes *Nature Commun.* **3** 1278

[16] Mazilu M, Mourka A, Vettenburg T, Wright E M and Dholakia K 2012 Simultaneous determination of the constituent azimuthal and radial mode indices for light fields possessing orbital angular momentum *Appl. Phys. Lett.* **100** 231115

[17] Hickmann J M, Fonseca E J S, Soares W C and Chávez-Cerda S 2010 Unveiling a truncated optical lattice associated with a triangular aperture using light's orbital angular momentum *Phys. Rev. Lett.* **105** 053904

[18] Mourka A, Baumgartl J, Shanor C, Dholakia K and Wright E M 2011 Visualization of the birth of an optical vortex using diffraction from a triangular aperture *Opt. Express* **19** 5760–71

[19] Courtial J, Dholakia K, Robertson D A, Allen L and Padgett M J 1998 Measurement of the rotational frequency shift imparted to a rotating light beam possessing orbital angular momentum *Phys. Rev. Lett.* **80** 3217–9

[20] Allen L, Babiker M and Power W L 1994 Azimuthal Dopper-shift in light-beams with orbital angular momentum *Opt. Commun.* **112** 141–4

[21] Vasnetsov M V, Torres J P, Petrov D V and Torner L 2003 Observation of the orbital angular momentum spectrum of a light beam *Opt. Lett.* **28** 2285–7

[22] Lavery M P J, Dudley A, Forbes A, Courtial J and Padgett M J 2011 Robust interferometer for the routing of light beams carrying orbital angular momentum *New J. Phys.* **13** 093014

[23] Berkhout G C G, Lavery M P J, Courtial J, Beijersbergen M W and Padgett M J 2010 Efficient sorting of orbital angular momentum states of light *Phys. Rev. Lett.* **105** 153601

[24] Lavery M P J, Robertson D J, Berkhout G C G, Love G D, Padgett M J and Courtial J 2012 Refractive elements for the measurement of the orbital angular momentum of a single photon *Opt. Express* **20** 2110–5

[25] Dudley A, Mhlanga T, Lavery M, McDonald A, Roux F S, Padgett M J and Forbes A 2013 Efficient sorting of Bessel beams *Opt. Express* **21** 165–71

[26] Lavery M P J, Robertson D J, Sponselli A, Courtial J, Steinhoff N K, Tyler G A, Wilner A and Padgett M J 2013 Efficient measurement of orbital angular momentum over 50 states *New J. Phys.* **15** 013024

[27] Dudley A, Litvin I A and Forbes A 2012 Quantitative measurement of the orbital angular momentum density of light *Appl. Opt.* **51** 823–33

[28] Torner L, Torres J P and Carrasco S 2005 Digital spiral imaging *Opt. Express* **13** 873–81

[29] Rodrigo J A, Caravaca-Aguirre A M, Alieva T, Cristobal G and Calvo M L 2011 Microparticle movements in optical funnels and pods *Opt. Express* **19** 5232–43

[30] Hodgson N and Weber H 2005 *Laser Resonators and Beam Propagation* (Berlin: Springer)

[31] Snyder A W and Love J D 1996 *Optical Waveguide Theory* (London: Chapman and Hall)

[32] Schulze C, Naidoo D, Flamm D, Schmidt O A, Forbes A and Duparré M 2012 Wavefront reconstruction by modal decomposition *Opt. Express* **20** 19714–25

[33] Schulze C, Ngcobo S, Duparré M and Forbes A 2012 Modal decomposition without *a priori* scale information *Opt. Express* **20** 27866–73

[34] Flamm D, Naidoo D, Schulze C, Forbes A and Duparré M 2012 Mode analysis with a spatial light modulator as a correlation filter *Opt. Lett.* **37** 2478–80

[35] Kaiser T, Flamm D, Schröter S and Duparré M 2009 Complete modal decomposition for optical fibers using CGH-based correlation filters *Opt. Express* **17** 9347–56

[36] Golub M A, Prokhorov A M, Sisakian I N and Soifer V A 1982 Synthesis of spatial filters for investigation of the transverse mode composition of coherent radiation *Sov. J. Quantum Electron.* **12** 1208–9

[37] Goodman J W 1968 *Introduction to Fourier Optics* (New York: McGraw-Hill)

[38] Arrizón V, Ruiz U, Carrada R and González L A 2007 Pixelated phase computer holograms for the accurate encoding of scalar complex fields *J. Opt. Soc. Am.* A **24** 3500–7

[39] Lee W-H 1979 Binary computer-generated holograms *Appl. Opt.* **18** 3661–9

[40] Born M and Wolf E 1991 *Principles of Optics* (Cambridge: Cambridge University Press)

[41] Berry H G, Gabrielse G and Livingston A E 1977 Measurement of the Stokes parameters of light *Appl. Opt.* **16** 3200–5

[42] Flamm D, Schmidt O A, Schulze C, Borchardt J, Kaiser T, Schröter S and Duparré M 2010 Measuring the spatial polarization distribution of multimode beams emerging from passive step-index large-mode-area fibers *Opt. Lett.* **35** 3429–31

[43] Litvin I A, Dudley A and Forbes A 2011 Poynting vector and orbital angular momentum density of superpositions of Bessel beams *Opt. Express* **19** 16760–71

[44] Aiello A, Lindlein N, Marquardt C and Leuchs G 2009 Transverse angular momentum and geometric spin Hall effect of light *Phys. Rev. Lett.* **103** 100401

[45] Soskin M S, Gorshkov V N, Vasnetsov M V, Malos J T and Heckenberg N R 1997 Topological charge and angular momentum of light beams carrying optical vortices *Phys. Rev.* A **56** 4064–75

[46] Baumann S M, Kalb D M, MacMillan L H and Galvez E J 2009 Propagation dynamics of optical vortices due to Gouy phase *Opt. Express* **17** 9818–27

[47] Allen L and Padgett M J 2000 The Poynting vector in Laguerre–Gaussian beams and the interpretation of their angular momentum density *Opt. Commun.* **184** 67–71

[48] Leach J, Keen S, Padgett M J, Saunter C and Love G D 2006 Direct measurement of the skew angle of the Poynting vector in a helically phased beam *Opt. Express* **14** 11919–24

[49] Bozinovic N, Golowich S, Kristensen P and Ramachandran S 2012 Control of orbital angular momentum of light with optical fibers *Opt. Lett.* **37** 2451–3

[50] Flamm D, Schulze C, Naidoo D, Schröter S, Forbes A and Duparré M 2013 All-digital holographic tool for mode excitation and analysis in optical fibers *J. Light. Technol.* **31** 1023–32